Karhunen-Loève Transform for Compressive Sampling Hyperspectral Images

Lei Liu[a,b], Jingwen Yan[c], Xianwei Zheng[b],Hong Peng[c], Di Guo[d], Xiaobo Qu[e*]

[a]Shantou University, Medical College, Shantou 515063, China

[b]Shantou University, Department of Mathematics, Shantou 515063, China

[c]Shantou University, Guangdong Provincial Key Laboratory of Digital Signal and Image Processing Techniques, Department of Electrical Engineering, Shantou 515063, China

[d]Xiamen University of Technology, School of Computer and Information Engineering, Fujian Provincial University Key Laboratory of Internet of Things Application Technology, Xiamen 361024, China

[e]Xiamen University, Department of Electronic Science, Xiamen 361005, China

***Corresponding author**: Xiaobo Qu, E-Mail: quxiaobo@xmu.edu.cn.

Citation: Lei Liu, Jingwen Yan, Xianwei Zheng, Hong Peng, Di Guo, Xiaobo Qu*. Karhunen-Loève transform for compressive sampling hyperspectral images, Optical Engineering, 54(1): 014106, doi:10.1117/1.OE.54.1.014106, 2015.

You can view it online at http://dx.doi.org/10.1117/1.OE.54.1.014106

Abstract: Compressed sensing is a new jointly sampling and compression technology for remote sensing. In hyperspectral imaging, typical compressed sensing method encodes the 2D spatial information of each spectral band or encodes the 3rd spectral information simultaneously. However, encode the spatial information is much easier than spectral information. Therefore, it is crucial to make use of spectral information to improve the compression rate on 2D compressed sensing data. In this paper, we propose to encode the 3rd spectral information with adaptive Karhunen-Loève transform. With a mathematical proof, we show that inter-spectral correlations are preserved among 2D randomly encoded spatial information. This property gives that one can compress 2D compressed sensing data effectively with Karhunen-Loève transform. Experiments demonstrate that the proposed method can better reconstruct both spectral curves and spatial images than traditional compression methods at the bit rates 0~1.

Keywords: hyperspectral images; compressive sensing; compression; Karhunen-Loève transform.

1 Introduction

Hyperspectral images (HSI) have high-resolution in both spectral and spatial. These data are acquired on satellites or aerospace sensors, and are used for many applications, such as geological surveys, military and environmental monitoring, etc. However, sensors and equipment hardware resources are extremely limited on satellites and aerospace. The huge amounts of data restrict the transmission and storage of hyperspectral images [1]. Data compression, which improves the transmission efficiency, is one of the most important methods for solving such conflicts.

Hyperspectral images compression can be roughly classified into two major categories: lossless and lossy compressions. The lossless compression techniques for hyperspectral data are typical prediction based on approaches [2-4], but compression ratio is generally only from 2 to 5 [5]. Lossy compression allows for much higher compression ratios than lossless one, where the lossy one leads to adequate reconstruction fidelity for many applications. The discrete cosine transform and the discrete wavelet transform (DWT) are used widely in compression method to make the energy of spatial dimension compact. They have been extended to 3D-discrete cosine transform [6, 7] and 3D-DWT [8, 9] for 3D HSI data compression. Karhunen–Loève (KL) transform is a classic method to remove the spectral redundancy in 3D HSI data and has been applied to compress data into few principal components. In the sense of minimum mean square error, KL transform is optimal and the most effective technique for data decorrelation [10, 11]. KL transform has been successfully employed in conjunction with wavelet transform to compress hyperspectral images, such as KL with JPEG2000 [12-14]. Considering the tree structure of wavelet coefficients, the 3D set partitioning in hierarchical trees (3D-SPIHT)

with wavelet in the spatial domain and KL in the spectral domain were employed to improve the compression rate [15, 16].

The traditional compression methods have achieved promising results but still have two major drawbacks:

1) The Nyquist sampling rule must be satisfied before performing lossy compression. This implies that some of these data are discarded in the lossy compression stage. Besides that, keeping these data before compression requires storage resources.
2) Compressing hyperspectral data on board requires hardware and software resources which are usually very limited in satellites and aerospace remote sensing equipment.

Can we find an effective way of sampling which simultaneously performs data compressing? If it is possible, this method is not only simple in the coding side on satellites and aerospace remote sensing equipment, but also reduces the amount of data and storage space while improving the transmission efficiency and the utilization efficiency of the sensors.

Compressed sensing (CS) [17, 18] has been proposed to solve these contradictions potentially. The hyperspectral images are acquired compressively by sensors based on the theory of CS. This new technology has been applied in remote sensing and showed promising results[19, 20]. Duarte *et al.* [21] and Ma [22] proposed a single-pixel imaging method in order to reduce number of sensors, respectively. Soldevila *et al.* [23] proposed a single-pixel optical system in polarimetric spectral imaging. Wagadarikar 24 proposed a coded aperture snapshot spectral imaging (CASSI) system in which the measurements are coded following the compressive sensing theory. T. Sun25 discussed the advantage of compressed sensing hyperspectral imager. Aravind *et al.* [26] used ten spectral bands to compare orthogonal matching pursuit with simultaneous orthogonal matching pursuit in

reconstruction. Huo *et al.* [27] proposed a technique, compressing hyperspectral images with the CS sampling, to reduce the data size further. Typical CS hyperspectral imaging encodes the 2D spatial information separately or encoding the 3rd spectral information simultaneously. However, encode the spatial information is much easier than spectral information. Therefore, it is crucial to make use of spectral information to improve the compression rate on 2D compressed sensing data.

In this paper, using encoding the 3rd spectral information with adaptive Karhunen-Loève (KL) transform, we discuss how to improve the compression rate under the framework of CS. By a mathematical proof, we show that inter-spectral correlations are preserved among 2D randomly encoded spatial information. This property gives that one can compress 2D compressed sensing data effectively with Karhunen-Loève transform. Two steps are designed in our compression method. First, a spatial image is under-sampled by CS encoding matrix. Second, the adaptive KL transform is used to provide spectral structure sparsity priors, and the transform removes the spectral correlations of undersampled measurements. Our method is wolves both CS and adaptive KL transform, thus we call it CSAKL for short. Applying the experiments, we obtain that CSAKL is advantaged of than typical CS and wavelet-based HSI compression methods.

This paper is organized as follows. In Sec. 2, compressive encoding and decoding in spatial and spectral are introduced. The experimental results are discussed in Sec. 3. In the last section, conclusions are given.

2 Adaptive KL transform on the compressive samples

Fig. 1 Flow chart of the proposed method

In this section, the new lossy compression recovery method CSAKL is designed. CSAKL performs compressive sensing in the spatial dimension and adaptive KL transform in spectral dimension. A fast iterative shrinkage-thresholding algorithm [28, 29] is used to reconstruct HSI data from undersampled samples. Fig. 1 shows a flow chart of the proposed method.

2.1 Compressive encoding on the spatial dimension

The theory of CS shows that a sparse signal can be recovered from a relatively small number of linear measurements [17, 18]. For HSI data **x,** we can perceive the spatial domain compressed HSI data by an orthogonalizable Gaussian random matrix **Φ** according to the CS theory. Let HSI $\mathbf{x}=(\mathbf{x}^{(1)}, \mathbf{x}^{(2)}, \cdots, \mathbf{x}^{(L)}) \in \mathbb{R}^{M\times N\times L}$, where $\mathbf{x}^{(i)}$ is the i^{th} spectral band image, $M\times N$ represent the spatial dimensions and L represents the spectral depth of HSI. Let $\mathbf{x}_i$ be a column vector of the i^{th} band HSI with size $MN\times 1$, $\mathbf{x}=(\mathbf{x}_1, \mathbf{x}_2, \cdots, \mathbf{x}_L) \in \mathbb{R}^{MN\times L}$. In order to retain strong correlation between adjacent spectral bands, each spectral band is encoded separately with a same encoding matrix **Φ**. The data acquisition model for CS is given by

$$\mathbf{y}_i = \mathbf{\Phi}_i \mathbf{x}_i \tag{1}$$

$$\mathbf{Y} = [\mathbf{y}_1, \mathbf{y}_2, \cdots, \mathbf{y}_L] \tag{2}$$

where **Y** is compressive samples, $\mathbf{\Phi}_i \in \mathbb{R}^{J\times MN}$ $(J \ll MN)$ $(1\le i \le L)$ is an encoding matrix for the band i of HSI, $\mathbf{y}_i \in \mathbb{R}^{J\times 1}$ $(1\le i \le L)$ is the acquired spatial under-sampled data for the i^{th} band of HSI. The compressive sampling ratio (*CSR*) is defined as

$$CSR = \frac{J}{MN} \tag{3}$$

which is compression rate of the HSI data at spatial dimension. CS encodes every spectral band using Gaussian encoding matrix which leads $\mathbf{y}_i$ to be random. Thus, it is

difficult to compress single $\mathbf{y}_i$ with wavelet or other transform. Fortunately, compress all $\mathbf{y}_i \left(i = 1, 2, \cdots, L\right)$ jointly is possible if the redundancy is existed among spectral bands.

2.2 Adaptive KL Transform Encoding on Spectral Domain

2.2.1 Spectral correlations of the CS encoding data with 2D or 3D CS encoding matrix

There are two different acquisition schemes in CS HSI. When $\mathbf{\Phi}_i = \mathbf{\Phi}_j$ $(i \neq j)$, each spectral band is encoded separately with a same encoding matrix, which is called 2D CS encoding matrix. When $\mathbf{\Phi}_i \neq \mathbf{\Phi}_j$ $(i \neq j)$, each spectral band is encoded separately with the different encoding matrix, which is called 3D CS encoding matrix. 3D CS encoding allows to reconstructing data better than 2D CS encoding [30] because of the randomness introduced along the spectral dimension. However, as is seen in Fig. 2, 3D CS encoding damages the correlation among spectral bands. This reduces the compression ratio for jointly compressing spectral bands. But this correlation can be well preserved by 2D CS encoding. Although it will be hard to prove the quantative relationship of correlations before and after the random encoding, one can evaluate the performance on the tested HSI data. Results in Fig.3 show that correlations after the random encoding is larger than that of the original signal. This observation is still held that different spatial compressive sampling ratios are used. Furthermore, it is difficult to implement in hardware for 3D encoding since different encoding matrices are required for different spectral bands. Therefore, 2D CS encoding scheme is adopted in this paper.

Fig. 2 The correlations of neighbouring spectral bands. (a)-(c) the correlations before the 2D CS encoding for Moffett, Cuprite and Lunar lake data, (d)-(f) the correlations after the 2D CS encoding for Moffett, Cuprite and Lunar lake data. (g)-(i) the correlations after the 3D CS encoding for Moffett, Cuprite and Lunar lake data. Note: The spatial compressive sampling ratios (*CSR*) is 50%。

Fig.3 The correlations of 2D CS encoding data with different *CSR*s. Note: Test is performed on $64\times64\times224$ Moffett dataset.

In the following, a mathematical proof is given to show that the 2D CS encoding scheme can preserve the inter-spectral correlations.

Definition 1 If $\boldsymbol{x}$ and $\boldsymbol{y}$ are nonzero and jointly distributed random variables, then the correlation coefficient of $\boldsymbol{x}$ and $\boldsymbol{y}$, denoted by $\rho(\boldsymbol{x}, \boldsymbol{y})$, is

$$\rho(\boldsymbol{x}, \boldsymbol{y}) = \frac{Cov(\boldsymbol{x}, \boldsymbol{y})}{\sqrt{Var(\boldsymbol{x})Var(\boldsymbol{y})}} \tag{4}$$

where $Cov(\boldsymbol{x}, \boldsymbol{y})$ is the covariance of $\boldsymbol{x}$ and $\boldsymbol{y}$, $Var(\cdot)$ is the variance of a random variable. We recall an important result from reference 31 as follows:

Lemma 1. The correlation coefficient of $\boldsymbol{x}$ and $\boldsymbol{y}$ satisfies $-1 \le \rho(\boldsymbol{x}, \boldsymbol{y}) \le 1$.

Furthermore, $\rho(\boldsymbol{x}, \boldsymbol{y}) = \pm 1$ if and only if $\mathrm{P}(\boldsymbol{y} = a + b\boldsymbol{x}) = 1$ for some constants a and b.

Next, we prove an auxiliary result.

Lemma 2. Let $\boldsymbol{x}, \boldsymbol{y} \in \mathbb{R}^{N\times1}$ be two strongly correlated vectors. The correlation coefficient of them is defined as

$$\rho(\boldsymbol{x}, \boldsymbol{y}) = \frac{\sum_{i=1}^{N}\left(x_i - \bar{x}\right)\left(y_i - \bar{y}\right)}{\sqrt{\sum_{i=1}^{N}\left(x_i - \bar{x}\right)^2 \sum_{i=1}^{N}\left(y_i - \bar{y}\right)^2}},$$

where $\boldsymbol{x}=(x_1, x_2, \cdots, x_N)^T$, $\boldsymbol{y}=(y_1, y_2, \cdots, y_N)^T$, $x_i, y_i \in [0,1]$ and $\bar{x}$ is the mean of $\boldsymbol{x}$, $\bar{y}$ is the mean of $\boldsymbol{y}$. Let $\boldsymbol{\Phi}$ be an orthogonal random matrix subjecting to normal distribution with mean 0 and variance 1, then $\rho(\boldsymbol{\Phi x}, \boldsymbol{\Phi y}) \approx 1$.

Proof. For vectors $\boldsymbol{x}, \boldsymbol{y} \in R^{N\times1}$, we have

$$\rho(\boldsymbol{x},\boldsymbol{y})=\frac{\langle \boldsymbol{x},\boldsymbol{y}\rangle-\bar{y}\sum_{i=1}^{N}x_i-\bar{x}\sum_{i=1}^{N}y_i+N\bar{x}\bar{y}}{\sqrt{\left(\langle \boldsymbol{x},\boldsymbol{x}\rangle-2\bar{x}\sum_{i=1}^{N}x_i+N\bar{x}^2\right)\left(\langle \boldsymbol{y},\boldsymbol{y}\rangle-2\bar{y}\sum_{i=1}^{N}y_i+N\bar{y}^2\right)}}$$

$$=\frac{\langle \boldsymbol{x},\boldsymbol{y}\rangle-\frac{1}{N}\sum_{i=1}^{N}x_i\sum_{i=1}^{N}y_i}{\sqrt{\left(\langle \boldsymbol{x},\boldsymbol{x}\rangle-\frac{1}{N}\left(\sum_{i=1}^{N}x_i\right)^2\right)\left(\langle \boldsymbol{y},\boldsymbol{y}\rangle-\frac{1}{N}\left(\sum_{i=1}^{N}y_i\right)^2\right)}},$$

where $\langle \boldsymbol{x},\boldsymbol{y}\rangle$ denotes the inner product of vectors $\boldsymbol{x},\boldsymbol{y}\in R^{N\times 1}$. Hence,

$$\rho(\boldsymbol{\Phi x},\boldsymbol{\Phi y})=\frac{\langle \boldsymbol{\Phi x},\boldsymbol{\Phi y}\rangle-\frac{1}{N}\sum_{i=1}^{N}(\boldsymbol{\Phi x})_i\sum_{i=1}^{N}(\boldsymbol{\Phi y})_i}{\sqrt{\left(\langle \boldsymbol{\Phi x},\boldsymbol{\Phi x}\rangle-\frac{1}{N}\left(\sum_{i=1}^{N}(\boldsymbol{\Phi x})_i\right)^2\right)\left(\langle \boldsymbol{\Phi y},\boldsymbol{\Phi y}\rangle-\frac{1}{N}\left(\sum_{i=1}^{N}(\boldsymbol{\Phi y})_i\right)^2\right)}}$$

$$=\frac{\langle \boldsymbol{\Phi}'\boldsymbol{\Phi x},\boldsymbol{y}\rangle-\frac{1}{N}\sum_{i=1}^{N}(\boldsymbol{\Phi x})_i\sum_{i=1}^{N}(\boldsymbol{\Phi y})_i}{\sqrt{\left(\langle \boldsymbol{\Phi}'\boldsymbol{\Phi x},\boldsymbol{x}\rangle-\frac{1}{N}\left(\sum_{i=1}^{N}(\boldsymbol{\Phi x})_i\right)^2\right)\left(\langle \boldsymbol{\Phi}'\boldsymbol{\Phi y},\boldsymbol{y}\rangle-\frac{1}{N}\left(\sum_{i=1}^{N}(\boldsymbol{\Phi y})_i\right)^2\right)}}$$

where $\boldsymbol{\Phi}$ is an orthogonal random matrix subjecting to normal distribution with mean zero and variance 1 and $\boldsymbol{\Phi}'\boldsymbol{\Phi}=\mathbf{I}$. The modulus of elements in $\boldsymbol{\Phi}$ are close sufficiently to zero when the dimension of $\boldsymbol{\Phi}$ is large enough. Therefore, $\boldsymbol{\Phi}$ is perturbation of a zero matrix. Since $\boldsymbol{\Phi}$ can be considered as a continuous linear operator and acts on $l^1(N)$ stably, $\sum_{i=1}^{N}(\boldsymbol{\Phi x})_i$ and $\sum_{i=1}^{N}(\boldsymbol{\Phi y})_i$ are sufficiently close to zero.

Note that the Cauchy-Schwart inequality, $|\langle \boldsymbol{x},\mathbf{y}\rangle|\le\sqrt{\langle \boldsymbol{x},\boldsymbol{x}\rangle\langle \mathbf{y},\mathbf{y}\rangle}$. Here the equation holds if and only if $\boldsymbol{x},\mathbf{y}$ are linear dependant. If the strong correlations lie in $\boldsymbol{x}$ and $\boldsymbol{y}$, then $|\langle \boldsymbol{x},\mathbf{y}\rangle|\approx\sqrt{\langle \boldsymbol{x},\boldsymbol{x}\rangle\langle \mathbf{y},\mathbf{y}\rangle}$. Thus

$$\rho(\boldsymbol{\Phi x},\boldsymbol{\Phi y})\approx\frac{\langle \boldsymbol{x},\boldsymbol{y}\rangle}{\sqrt{\langle \boldsymbol{x},\boldsymbol{x}\rangle\langle \boldsymbol{y},\boldsymbol{y}\rangle}}\approx 1. \qquad \#$$

Theorem 1. Suppose that $\mathbf{x} \in \mathbb{R}^{M\times N\times L}$ is a three-dimensional digital signal. $\mathbf{x}$ can be converted into two-dimensional digital signal $\mathbf{x}=(\boldsymbol{x}_1, \boldsymbol{x}_2, \cdots, \boldsymbol{x}_L) \in \mathbb{R}^{MN\times L}$, where $\boldsymbol{x}_i$, i=1, 2,$\cdots$, N, are MN-dimensional column vectors. $\mathbf{Y}=(\mathbf{y}_1, \mathbf{y}_2, \cdots, \mathbf{y}_L)$ is the measure data satisfied $\mathbf{Y} = \mathbf{\Phi x}$, where $\mathbf{\Phi}$ is a random encoding matrix. If strong correlations lie in adjacent spectral bands of **x,** then they also lie in **Y**.

Proof: Let the correlation coefficient between the i^{th} and the $(i+1)^{\text{th}}$ spectral bands for **x** be denoted by $R_{\mathbf{x}_i}$. If $R_{\mathbf{x}_i}=1$, by Lemma 1, there are some constants a_i and b_i, such that, $\mathrm{P}(\boldsymbol{x}_i = a_i\boldsymbol{x}_{i+1} + b_i) = 1$ for any i. Namely $\mathrm{P}(\mathbf{\Phi}\boldsymbol{x}_i = \mathbf{\Phi}(a_i\boldsymbol{x}_{i+1} + b_i)) = 1$. By the assumptions,

$$\mathrm{P}(\mathbf{\Phi}\boldsymbol{x}_i = \mathbf{\Phi}(a_i\boldsymbol{x}_{i+1} + b_i)) = \mathrm{P}(\boldsymbol{y}_i = a_i\boldsymbol{y}_{i+1} + \mathbf{\Phi}b_i)$$

that is, $\mathrm{P}(\boldsymbol{y}_i = a_i\boldsymbol{y}_{i+1} + \mathbf{\Phi}b_i) = 1$. By Lemma 1 again, $\rho(\boldsymbol{y}_i, \boldsymbol{y}_{i+1}) = 1$, for any i.

If strong correlations lie in adjacent spectral bands of **x,** then by Lemma 2, we have

$\rho(\boldsymbol{y}_i, \boldsymbol{y}_{i+1}) = \rho(\mathbf{\Phi}\boldsymbol{x}_i, \mathbf{\Phi}\boldsymbol{x}_{i+1}) \approx \dfrac{\langle \boldsymbol{x}_i, \boldsymbol{x}_{i+1}\rangle}{\sqrt{\langle \boldsymbol{x}_i, \boldsymbol{x}_i\rangle\langle \boldsymbol{x}_{i+1}, \boldsymbol{x}_{i+1}\rangle}} \approx 1$ .Thus, the neighbouring spectral bands of **Y** are strongly correlated. #

2.2.2 Adaptive KL compressive encoding with 2D CS encoding

According to the above analysis, strong correlations will be retained if each spectral band is encoded with the same random matrix. Now, we discuss how to compress these compressive samples.

The KL transform is the optimal technique for data decorrelation in the sense of minimum mean square error [14, 32]. KL transform makes the energy compact into few principal components along the spectral dimension. It is the eigenvalue decomposition

of the covariance matrices according to the following formula. Covariance matrix C of HSI data is given by

$$\mathbf{C} = \frac{1}{L}\sum_{i=1}^{L}(\mathbf{x}_i - \overline{\mathbf{x}})(\mathbf{x}_i - \overline{\mathbf{x}})^T \tag{5}$$

$$\mathbf{C}_g = \mathbf{A}\mathbf{C}\mathbf{A}^T \tag{6}$$

where $\mathbf{x}_i$ denotes the i^{th} spatial image of data $\mathbf{x}$ and $\overline{\mathbf{x}} = \sum_{i=1}^{L}\frac{\mathbf{x}_i}{L}$ is the means of data $\mathbf{x}$ in spectrum. Eigen decomposition is adopted for covariance matrix $\mathbf{C}$. $\mathbf{C}_g$ is a diagonal matrix. Let $\mathbf{C}_g(i,i)=\lambda_i$ $(1 \le i \le L)$ be an eigenvalue. $\mathbf{A}$ and $\mathbf{A}^T$ are normalized orthogonal eigenvectors and its transpose. Different spatial block have different normalized orthogonal eigenvectors $\mathbf{A}$. Following the formula, we can select eigenvalues and their corresponding eigenvectors such that the saved energy approaches above 99%.

$$\frac{\sum_{i=1}^{n}\lambda_i^2}{\sum_{i=1}^{L}\lambda_i^2} \ge 99\% \qquad 1 \le \mathrm{n} \le L \tag{7}$$

According to the selected eigenvalues and their corresponding eigenvectors, the KL transform becomes

$$\tilde{\mathbf{x}} = \left[\mathbf{x}_1 - \overline{\mathbf{x}}, \mathbf{x}_2 - \overline{\mathbf{x}}, \cdots, \mathbf{x}_L - \overline{\mathbf{x}}\right], \tag{8}$$

$$\mathbf{P} = \mathbf{A}^T\tilde{\mathbf{x}}\ , \tag{9}$$

$$\tilde{\mathbf{x}} = \mathbf{A}\,\mathbf{P}\ , \tag{10}$$

$$\mathbf{x} = \left[\tilde{\mathbf{x}}_1 + \overline{\mathbf{x}}, \tilde{\mathbf{x}}_2 + \overline{\mathbf{x}}, \cdots, \tilde{\mathbf{x}}_L + \overline{\mathbf{x}}\right], \tag{11}$$

where matrix $\mathbf{P}$ denotes the KL transform matrix of zero mean HSI data. In size $Q \times m \times n$ HSI data compression, only spectral means vector (Q), principal components ($k \times m \times n$), and k eigenvectors ($Q \times k$) need to be saved after KL transform. The adaptive KL transform compression ratio (*KLR*) can be calculated by

$$KLR = \frac{Q + k \times m \times n + Q \times k}{Q \times m \times n} \tag{12}$$

where $m \times n$ represents the spatial block size, k is the number of retained eigenvalues , and Q is the number of the spectral bands. The compression bit rate (*BR*) of the proposed method can be calculated by:

$$BR = 16 \times \frac{\text{the number of pixels of the compressed image}}{\text{the number of pixels of the original image}} = 16 \times CSR \times KLR \tag{13}$$

Here *CSR* is the compression rate in spatial domain defined in Eq. (3) and *KLR* is the compression rate in spectral domain defined in Eq. (12).

2.3 Decoding

There are two steps in decoding on ground stations and the flow chart is shown in Fig. 4. First, an inverse KL transform is performed with Eq. (6), (7)-(11) to recover CS undersampled HSI data. Second, a numerical algorithm to solve l_1 norm minimization problem is applied to reconstruct HSI data from undersampled samples using 3D wavelet transform, a typical sparse transform for HSI [33, 34]. Let $\mathbf{\Psi}$ represent inverse 3D wavelet transform and let $\mathbf{\Psi}^T$ denote its forward transform. CS recovers $\mathbf{x}$ by solving

$$\hat{\boldsymbol{\alpha}} = \arg\min_{\boldsymbol{\alpha}} \left\{ \lambda \|\boldsymbol{\alpha}\|_1 + \|\mathbf{y} - \mathbf{\Phi}\mathbf{\Psi}\boldsymbol{\alpha}\|_2^2 \right\} \tag{14}$$

where $\boldsymbol{\alpha} = \mathbf{\Psi}^T \mathbf{x}$, $\|\cdot\|_p$ (p=1,2) stands for l_p -norm, and λ is the regularization parameter which determines the tradeoff between the sparsity and the data fidelity. λ=10^{-2} is empirically chosen to give optimal results. In this paper, a fast iterative shrinkage-thresholding algorithm [28, 29] is used to solve Eq. (14) because of its simplicity and classic method. The final output is reconstructed images $\hat{\mathbf{x}} = \mathbf{\Psi}\hat{\boldsymbol{\alpha}}$.

Fig. 4 Flow chart of decoding.

3 Experimental results

The 16-bit HSI data are obtained from U.S. AVRIS website, including Moffett Field, Cuprite and Lunar Lake. Those data contain 224 spectral bands with spatial size 64×64, which are named as Moffett, Cuprite and Lunar lake, respectively. Every pixel is encoded with 16-bit, and all data are normalized between [0, 1]. Experiments run on a dual core 2.5 GHz CPU laptop with 4 GB RAM.

To evaluate the performance, the every band peak signal-to-noise ratio (PSNR), average peak signal-to-noise ratio (APSNR) and entire data peak signal-to-noise ratio (EPSNR) [35, 36] are adopted as criteria to measure the reconstruction HSI data. Their definitions are

$$MSE(s) = \frac{1}{M \cdot N} \sum_{j=1}^{M} \sum_{i=1}^{N} \left(\hat{\mathbf{x}}(i, j, s) - \mathbf{x}(i, j, s) \right)^2 \tag{15}$$

$$PSNR(s) = 10 \log_{10} \left(\frac{\left(\max(\max(\hat{\mathbf{x}}(i, j, s))) \right)^2}{MSE(s)} \right) \tag{16}$$

$$APSNR = \frac{1}{L} \sum_{s=1}^{L} PSNR(s), \tag{17}$$

$$EPSNR = 10 \log_{10} \left(\frac{\left(\max(\hat{\mathbf{x}}(:)) \right)^2}{\frac{1}{L \cdot M \cdot N} \sum_{s=1}^{L} \sum_{j=1}^{M} \sum_{i=1}^{N} \left(\hat{\mathbf{x}}(i, j, s) - \mathbf{x}(i, j, s) \right)^2} \right) \tag{18}$$

where $\mathbf{x}$ denotes the original HSI cube data, and $\hat{\mathbf{x}}$ denotes the recovered HSI cube data, s denotes the number of spectral bands. APSNR can evaluate the average reconstruction performance of each band while EPSNR evaluates the whole reconstruction performance that is regardless of the spectral bands.

3.1 Eigenvalues of 2D CS samples

For a certain spatial position in a hyperspectral images, there are a number of different bands. Therefore, the similarity between the adjacent spectrum segments is more prominent, which leads to the high correlation between adjacent spectral images. This correlation is also known as the spectral structure. After 2D CS encoding, the spectral structure has not changed, as shown in Fig. 2(d)-(f). Except a few spectral bands, the spectral correlation coefficients for other bands are above 0.95.

The attenuation of eigenvalues with adaptive KL transform on three HSI data is tested in Fig. 5 (a). The eigenvalues of the covariance have obvious attenuation with $\lambda_1 \gg \lambda_2 \geq \cdots \geq \lambda_L$ for three datasets. By preserving small number of eigenvalues, reconstruction errors for all data decay rapidly as is seen in Fig. 5 (b), where the normalized energy error $\frac{\left\|\hat{\mathbf{x}}-\mathbf{x}\right\|_2^2}{\left\|\mathbf{x}\right\|_2^2}$ is used as the reconstruction error. A faster decay of eigenvalues is observed on Lunar lake which contains strong edges and textures. By our method, for HSI data with fruitful edges and textures, a better reconstruction can be achieved.

Fig. 5 The attenuation curves of three types HSI CS encoding data. (a) Eigenvalues, (b) Reconstruction error. Note: The spatial compressive sampling ratios (*CSR*) is 50%。

The eigenvalues of CS encoding data covariance with different sampling rate shows obvious attenuation in Fig. 6. The energy of CS samples approaches above 99% when 2 eigenvalues are retained because of the correlations between spectral bands.

Fig. 6 The eigenvalues versus different sampling rate CS encoding data. Note: Test is performed on Moffett dataset.

3.2 The CSAKL method under different spatial compression rates

The total compression rate can be optimized if the compression rates in the spatial and spectral dimension are adjusted properly according to Eq. (13). The spectral compression is obtained by preserving a small number of eigenvalues and their corresponding eigenvectors for three types HSI data. In the future, higher compression rate may be achieved by cutting down random encoding rate in the spatial domain.

(A) Entire data cube PSNR

For the i^{th} spectral band image, the CS undersampling equation can be expressed as $\mathbf{y}_i = \mathbf{\Phi}_i \mathbf{x}_i$, where $\mathbf{x}_i \in \mathbb{R}^{64^2 \times 1}$, $\mathbf{\Phi}_i \in \mathbb{R}^{CSR \cdot 64^2 \times 64^2}$ and *CSR* is spatial compression rate. Spatial sampling rate *CSR* is 0.3, abbreviated as 30%. The same number of eigenvalues and their corresponding eigenvectors is selected, the reconstruction PSNR is compared under different spatial compression rate. As is shown in Fig. 7, by preserving two eigenvalues and their corresponding eigenvectors, spatial sampling compression rate have more influence in reconstructing EPSNR when *CSR* is smaller than 50%, but a little change in EPSNR when *CSR* is large than 60%. Thus, for *CSR* is smaller than 50%, more eigenvalues and their corresponding eigenvectors should be retained to enhance EPSNR.

Fig. 7 EPSNR performance under different spatial compression rates.

(B) Describe the different PSNR values for different band

The HSI data may contain different levels of noise in different bands, thus the EPSNR is not enough to discuss the compression performance regarding with these bands. In this case, PSNR for every band will be more meaningful to understand the relationship between *CSR* and quality of reconstructed image. PSNRs of every band with different spatial sampling compression rates are shown in Fig. 8. In Fig. 8, 40%, 50%, 60%, 70%,

80% indicate the *CSR* is 0.4, 0.5, 0.6, 0.7 and 0.8 respectively. For HSI data, water-absorption and noisy make information of about 35 noise bands (from 100 to 115 bands and 150 to 170 bands) junk. The reconstruction performance of the noise bands is much lower than other bands with very poor PSNR values. With the increase of *CSR*, we have observed the same increase in the PSNR curve. However, there are greater increases in PSNR curves when *CSR* is less than 50%. If *CSR* is over than 60%, the increase is slow.

Fig. 8 PSNRs performance under different spatial sampling compression rates. (a) Moffett, (b) Cuprite, (c) Lunar lake.

(C) Describe the average PSNR values for different band

The APSNR performance under different bit rates and spatial sampling compression rates is shown in Fig. 9. When *CSR* are 60%, 70% and 80%, the similar APSNR is received. Overall consideration, *CSR*=60% is selected as the best combination. This setting will be used to compare our method with other methods.

Fig. 9 APSNR of reconstruction image with different bit rate and spatial sampling compression rate. (a) Moffett, (b) Cuprite, (c) Lunar lake.

3.3 Comparison with typical compression methods

In this subsection, the proposed method CSAKL based on CS theory and adaptive KL transform, is compared with CSDWT, which adopts CS in spatial domain and DWT in spectral domain, and with the typical HSI compression method 3D SPIHT [37, 38]. The compression bit rate of CSAKL is proportional to the product of *CSR* and *KLR,* denoted by $BR=16\times CSR\times KLR$.

The average PSNRs under different bit rates are showed in Fig. 10. On the three datasets, the proposed CSAKL achieves better PSNRs performance than other two methods. The advantage is more obvious when the bit rate is lower than 0.6.

Fig. 10 APSNR with different compression bit rate. (a) Moffett, (b) Cuprite, (c) Lunar lake.

Structures of images (see in Fig. 11) are preserved better using CSAKL than using 3D SPIHT and CSDWT. For instance, SPIHT seriously blurs the images in Figs. 11 (d) - (f) and CSDWT presents noise-like artifacts in Figs. 11 (g) - (i)**.** These problems are not observed in the proposed method.

Reconstructed spectral lines are compared in Fig. 12. The points close to image edges are selected. The spectral curves are preserved much better using CSAKL than other methods. Too smoothen spectral lines are reconstructed with CSDWT. One reason to explain this is that only partial low-frequency coefficients are retained in DWT at low bit rate (0.3 bpp in this case).

Fig. 11 The reconstructed 135^{th} band of test HSI data using CSDWT, 3D-SPIHT, and CSAKL when BR=0.3bpp. (a)-(c) are the 135^{th} original Moffett, Cuprite and Lunar lake datasets, (d)-(f) are reconstruction using 3D-SPIHT, the PSNRs are 21.35dB, 28.05dB, 29.87dB, (g)-(i) are reconstruction using CSDWT, the PSNRs are 23.15dB, 34.35dB, 33.44dB, (j)-(l) are reconstruction using CSAKL, the PSNRs are 34.65dB, 38.80dB, 37.28dB respectively.

Fig. 12 Recovered spectral line using 3D SPIHT, CSDWT and CSAKL when BR=0.3 bpp. (a) Moffett, spatial position (37, 55), (b) Cuprite, spatial position (25, 38), (c) Lunar lake, spatial position (55, 51).

4 Conclusions

Compressive sensing is a new sampling and compression technology for hyperspectral imaging. In this paper, we proved that inter-spectral correlations are preserved among 2D compressive sensing hyperspectral imaging data. Correspondingly, adaptive Karhunen-Loève transform is proposed to remove the spectral redundancy of spatially encoded data such that improve the compression performance is improved. Experiments demonstrate that the proposed method has better reconstruction performances on both

spectral cures and spatial images than traditional compression methods. In the future, proving the quantative relationship of correlations before and after the random encoding will improve the theoretical foundation of this paper. We also plan to design effective CS encoding matrix in the spatial dimension to provide sparse representation of HSI images, including optimizing sparse representation of HSI, e.g. geometric direction sparse representation [39, 40] and self-similarity [41-43]. Besides, how to adjust the compression rates in the spatial and spectral dimension to achieve higher overall compression rates is still open.

Acknowledgments

The authors are grateful to the reviewers for their thorough review. This work was supported in part by the National Natural Science Foundation of China (61201045, 40971206 and 61302174), Fundamental Research Funds for the Central Universities (2013SH002), Open Fund from Key Lab of Digital Signal and Image Processing of Guangdong Province (54600321 and 2013GDDSIPL-07), Academic Innovation Team Building Project of Shantou University (ITC12002), and Scientific Research Foundation for the Introduction of Talent at Xiamen University of Technology (90030606).

References

1. R. B. Gomez, "Hyperspectral imaging: a useful technology for transportation analysis," *Opt. Eng*. **41**(09), 2137- 2143 (2002).
2. F. Rizzo, B. Carpentieri, G. Motta, and J. A. Storer,"Low-complexity lossless compression of hyperspectral imagery via linear prediction," *IEEE Signal Proc. Let.* **12**(2), 138-141 (2005).

3. J. Mielikainen, P. Toivanen, and A. Kaarna," Linear prediction in lossless compression of hyperspectral images," *Opt. Eng*. **42**(04), 1013-1017 (2003).
4. R. Pizzolante, and B. Carpentieri, "Visualization, band ordering and compression of hyperspectral Images," *Algorithms*. **5**(1), 76-97 (2012).
5. J. Mielikainen, and P. Toivanen, "Lossless compression of hyperspectral images using a quantized index to lookup tables," *IEEE Geosci. Remote Sens. Lett.* **5**(3), 474-478 (2008).
6. G. P. Abousleman, M. W. Marcellin, and B. R. Hunt, "Compression of hyperspectral imagery using the 3-D DCT and hybrid DPCM/DCT," *IEEE Trans. Geosci. Remote Sens.* **33**(1), 26-34 (1995).
7. D. Markman, and D. Malah, "Hyperspectral image coding using 3D transforms," *2001 International Conference on Image Processing*. Thessaloniki (2001).
8. S. Lim, K. Sohn, and C. Lee,"Compression for hyperspectral images using three dimensional wavelet transform," *2001 IEEE International Geoscience and Remote Sensing Symposium (IGARSS'01).* Sydney, NSW (2001).
9. J. E. Fowler, and J. T. Rucker, "Three-dimensional wavelet-based compression of hyperspectral imagery," in *Hyperspectral Data Exploitation: Theory and Applications*, Chein-I. Chang, Ed, pp. 379-407, Hoboken, New Jersey (2007).
10. X. Kang, S. Li, and J. A. Benediktsson, "Spectral-spatial hyperspectral image classification with edge-preserving filtering", *IEEE Trans. Geosci. Remote Sens.* **52**(5), 2666-2677 (2014).
11. H. Li, L. Zhang, and H. Shen, "A principal component based Haze masking method for visible images," *IEEE Geosci. Remote Sens. Lett.* **11**(5), 975-979 (2014).

12. Q. Du, and J. E. Fowler, "Hyperspectral image compression using JPEG2000 and principal component analysis," *IEEE Geosci. Remote Sens. Lett.* **4**(2), 201-205 (2007).
13. Q. Du, and J. E. Fowler, "Low-complexity principal component analysis for hyperspectral image compression," *Int. J. High Perform. C.* **22**(4), 438-448 (2008).
14. B. Penna, T. Tillo, E. Magli, and G. Olmo,"A new low complexity KLT for lossy hyperspectral data compression," *Proceedings of the International Geoscience and Remote Sensing Symposium*. 7(06), 3508-3511 Denver, Co, USA (2006).
15. P. L. Dragotti, G. Poggi, and A. R. P. Ragozini, "Compression of multispectral images by three-dimensional SPIHT algorithm," *IEEE Trans. Geosci. Remote Sens.* **38**(1), 416-428 (2000).
16. X. Tang, S. Cho, and W. A. Pearlman,"3D set partitioning coding methods in hyperspectral image compression," *In IEEE International Conference on Image Processing (ICIP)*. Barcelona, Spain (2003).
17. E. J. Candès, J. Romberg, and T. Tao, "Robust uncertainty principles: Exact signal reconstruction from highly incomplete frequency information," *IEEE Trans. Inf. Theory*. **52**(2), 489-509 (2006).
18. D. L. Donoho, "Compressed sensing," *IEEE Trans. Inf. Theory*. **52**(4), 1289-1306 (2006).
19. H. Shen, X. Li, L. Zhang, D. Tao, and C. Zeng, "Compressed Sensing Based Inpainting of Aqua Moderate Resolution Imaging Spectroradiometer Band 6 Using Adaptive Spectrum-Weighted Sparse Bayesian Dictionary Learning," *IEEE Trans. Geosci. Remote Sens*. **52**(2), 894-906 (2013).
20. J.-F. Cai, H. Ji, F. Shang, and Z. Shen, "Inpainting for Compressed Images," *Appl. Comput. Harmon. Anal*. **29**(3): 368-381 (2010).

21. M. F. Duarte, M. A. Davenport, D. Takhar, and J. N. Laska, “Single-pixel imaging via compressive sampling,” *IEEE Signal Process. Mag.* **25**(2), 83-91 (2008).
22. J. Ma, “Single-pixel remote sensing,” *IEEE Geosci. Remote Sens. Lett.* **6**(2), 199-203(2009).
23. F. Soldevila, E. Irles, V. Durán, P. Clemente, M. Fernández-Alonso, E. Tajahuerce, *et al.*, "Single-pixel polarimetric imaging spectrometer by compressive sensing," *Applied Physics B*, **113**, 551-558(2013).
24. A. A. Wagadarikar, N. P. Pitsianis, X. Sun, and D. J. Brady, "Spectral image estimation for coded aperture snapshot spectral imagers," *Proc. SPIE*, **7076**, 707602–707602–15 (2008).
25. T. Sun, K. Kelly, "Compressive sensing hyperspectral imager," *Computational Optical Sensing and Imagi*ng, San Jose, California United States, October 13-15, CTuA5 (2009).
26. N. V. Aravind, K. Abhinandan, V. V. Acharya, and D. S. Sumam,"Comparison of OMP and SOMP in the reconstruction of compressively sensed hyperspectral images," *In Processing of IEEE Communications and Signal Processing (ICCSP).* Hamirpur, India (2011).
27. C. Huo, R. Zhang, and D. Yin, "Compression technique for compressed sensing hyperspectral images," *Int. J. Remote Sens.* **33**(5), 1586-1604 (2012).
28. I. Daubechies, M. Defrise, and C. De Mol, "An iterative thresholding algorithm for linear inverse problems with a sparsity constraint," *Commun. Pur. Appl. Math.* **57**(11), 1413-1457 (2004).
29. K. Bredies, and D.A. Lorenz, "Linear convergence of iterative soft-thresholding," *J. Fourier Anal. Appl.* **14**(5-6), 813-837 (2008).

30. L. Liu, J.Yan, D Guo, Y. Liu, and X. Qu, "Undersampled hyperspectral image reconstruction based on surfacelet transform," *Journal of Sensors*, http://www.hindawi.com/journals/js/aip/256391/ , in press, 2014.
31. J. Rice, *Mathematical statistics and data analysis.* 3th ed., Thomson Higher Education, Belmont, CA, USA (2006).
32. J. Yan, H. Sun, and S. Zhang, "A multispectral image data compression method based on KLT/DCT," *The Chinese Journals of Laser*. **B6**(2), 110-116 (1997).
33. S. Prasad, L. Wei, J. E. Fowler, and L.M. Bruce, "Information fusion in the redundant-wavelet-transform domain for noise-robust hyperspectral classification," *IEEE Trans. Geosci. Remote Sens*. **50**(9), 3474-3486 (2012).
34. A. Karami, M. Yazdi, and G. Mercier, "Compression of hyperspectral images using discrete wavelet transform and tucker decomposition," *IEEE J-STARS*. **5**(2), 444-450 (2012).
35. T. Akgun, Y. Altunbasak, and R. M. Mersereau, "Super-resolution reconstruction of hyperspectral images," *IEEE Transactions on Image Processing*, **14**, 1860-1875 (2005).
36. C. Tang, N.-M. Cheung, A. Ortega, and C. S. Raghavendra, "Efficient inter-band prediction and wavelet based compression for hyperspectral imagery: a distributed source coding approach," *Proceedings. DCC 2005,* 437-446(2005).
37. X. Tang, S. Cho, and W.A. Pearlman, "Comparison of 3D set partitioning methods in hyperspectral image compression featuring an improved 3D-SPIHT," *In Proceedings of IEEE Data Compression Conference,* Snowbird, UT, USA (2003).
38. B. J. Kim, Z. Xiong, and W.A. Pearlman, "Low bit-rate scalable video coding with 3-D set partitioning in hierarchical trees (3-D SPIHT)," *IEEE T. Circ. Syst. Vid.* **10**(8), 1374-1387 (2000).

39. Peyré G, Mallat S, "Surface compression with geometric bandelets," *ACM Trans. Graphic*. **24**(3), 601-608 (2005).

40. X. Qu, D. Guo, B. Ning, Y. Huo, Y. Lin, S. Cai, and Z. Chen, "Undersampled MRI reconstruction with patch-based directional wavelets," *Magn. Reson. Imaging*. **30**(7), 964-977 (2012).

41. M. Maggioni, V. Katkovnik, K. Egiazarian, and A. Foi, "Nonlocal transform-domain filter for volumetric data denoising and reconstruction," *IEEE Trans. Image Process.* 22(1), 119-133 (2013).

42. X. Qu, Y. Hou, F. Lam, D. Guo, J. Zhong, and Z. Chen, "Magnetic resonance image reconstruction from undersampled measurements using a patch-based nonlocal operator, " *Medical Image Analysis*, 18(6), 843-856 (2014).

43. X. Lei, W. Wu, Z. Liang, and X. He, "Single remote sensing image supper-resolution based on sparse representation theory with self-trained dictionary learning," *Journal of Computational Infor.* **8**(8), 3269–3283 (2012).

Caption List

Fig. 1 Flowchart of the proposed method.

Fig. 2 The correlations of neighbouring spectral bands. (a)-(c) the correlations before the 2D CS encoding for Moffett, Cuprite and Lunar lake data, (d)-(f) the correlations after the 2D CS encoding for Moffett, Cuprite and Lunar lake data. (g)-(i) the correlations after the 3D CS encoding for Moffett, Cuprite and Lunar lake data. Note: The spatial compressive sampling ratios (*CSR*) is 50%。

Fig.3 The correlations of 2D CS encoding data with different *CSR*s. Note: Test is performed on $64\times64\times224$ Moffett dataset.

Fig. 4 Flowchart of decoding process.

Fig. 5 The attenuation curves of three types HSI CS encoding data. (a) eigenvalues, (b) reconstruction error. Note: The spatial compressive sampling ratios (*CSR*) is 50%。

Fig. 6 The eigenvalues versus different sampling rate CS encoding data. Note: Test is performed on Moffett dataset.

Fig. 7 EPSNR performance under different spatial compression rates.

Fig. 8 PSNRs performance under different spatial sampling compression rates. (a) Moffett, (b) Cuprite, (c) Lunar lake.

Fig. 9 APSNR of reconstruction image with different bit rate and spatial sampling compression rate. (a) Moffett, (b) Cuprite, (c) Lunar lake.

Fig. 10 APSNR with different compression bit rate. (a) Moffett, (b) Cuprite, (c) Lunar lake.

Fig. 11 The reconstructed 135^{th} band of test HSI data using CSDWT, 3D-SPIHT, and CSAKL when BR=0.3bpp. (a) - (c) are the 135^{th} original Moffett, Cuprite and Lunar lake datasets, (d) - (f) are reconstruction using 3D-SPIHT, the PSNRs are 21.35dB,

28.05dB, 29.87dB, (g) - (i) are reconstruction using CSDWT, the PSNRs are 23.15dB, 34.35dB, 33.44dB, (j) - (l) are reconstruction using CSAKL, the PSNRs are 34.65dB, 38.80dB, 37.28dB respectively.

Fig. 12 Recovered spectral line using 3D SPIHT, CSDWT and CSAKL when BR=0.3 bpp. (a) Moffett, spatial position (37, 55), (b) Cuprite, spatial position (25, 38), (c) Lunar lake, spatial position (55, 51).

Fig.1

Satellites , aerospace

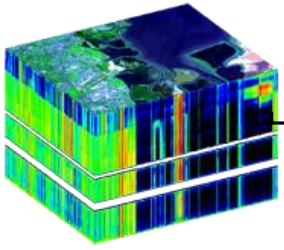

Encoding

sensor

Compressive encoding on spatial dimention

Adaptive KL transform on spectral dimention

Channel transmission

- Eigenvectors,
- Spectral means,
- Principal components

Receiving ground side

Inverse KL transform on spectral dimention

Sparse reconstruction on spatial dimention

Decoding

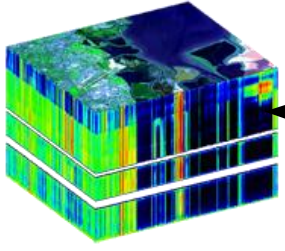

Groud Station

Fig.2

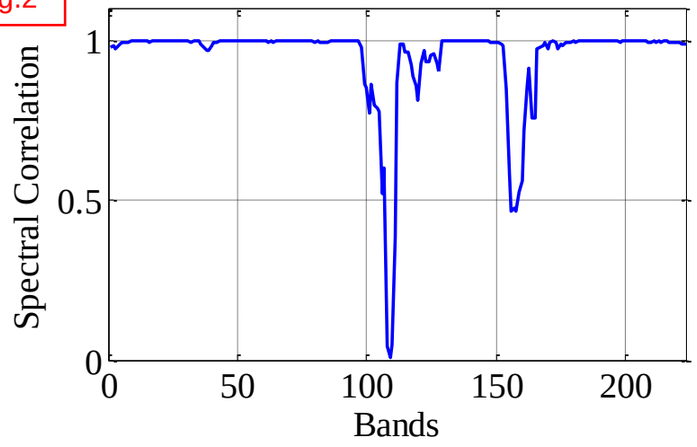

a

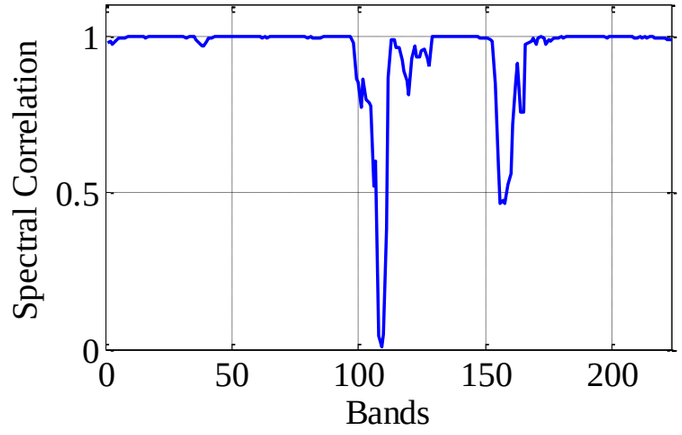

b

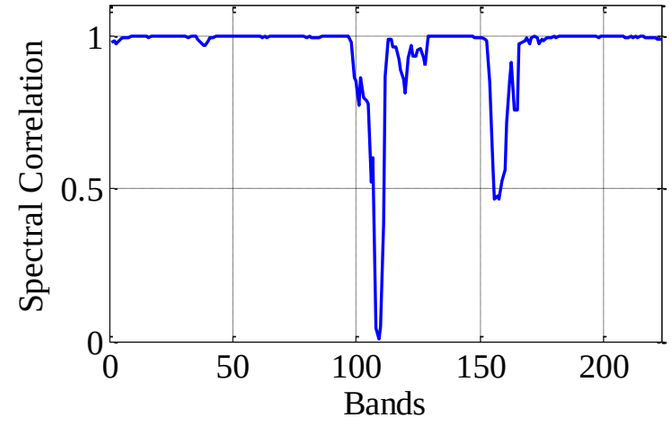

c

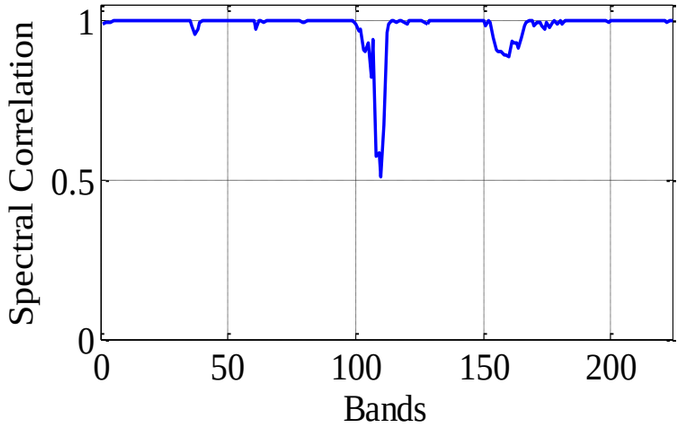

d

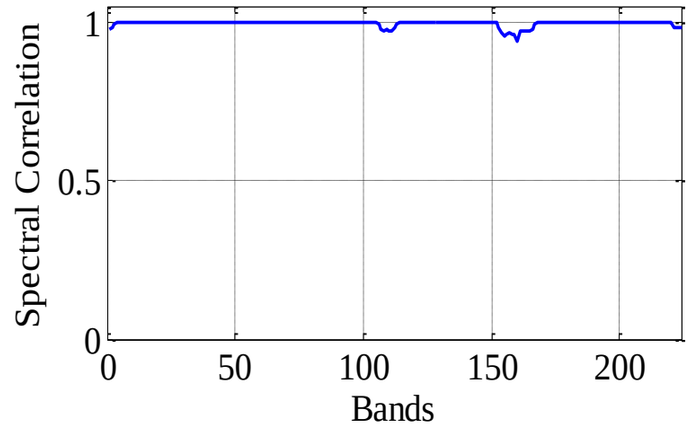

e

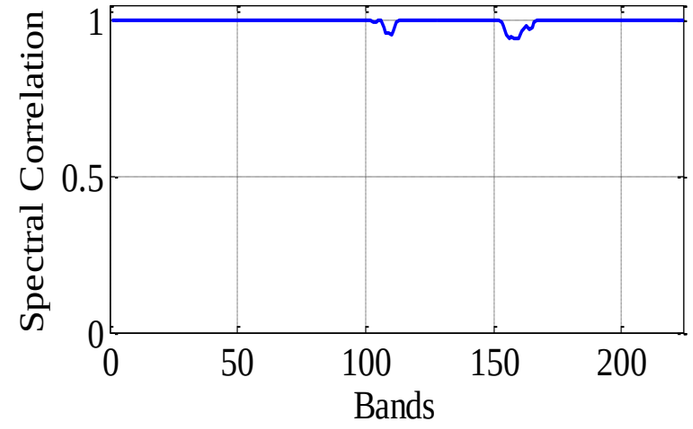

f

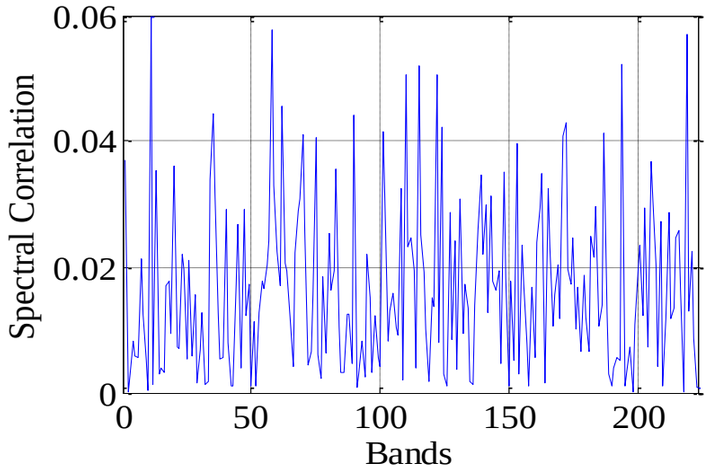

g

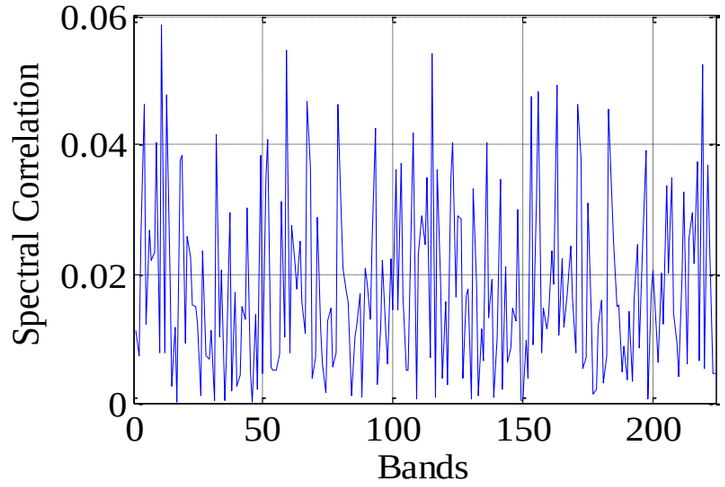

h

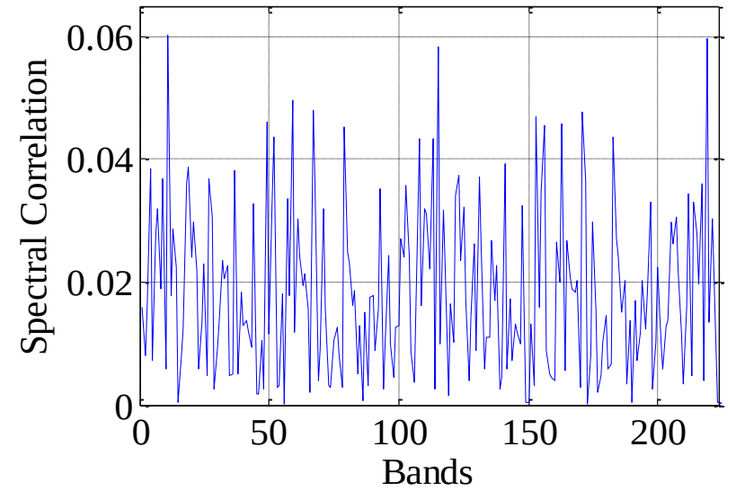

i

Fig.3

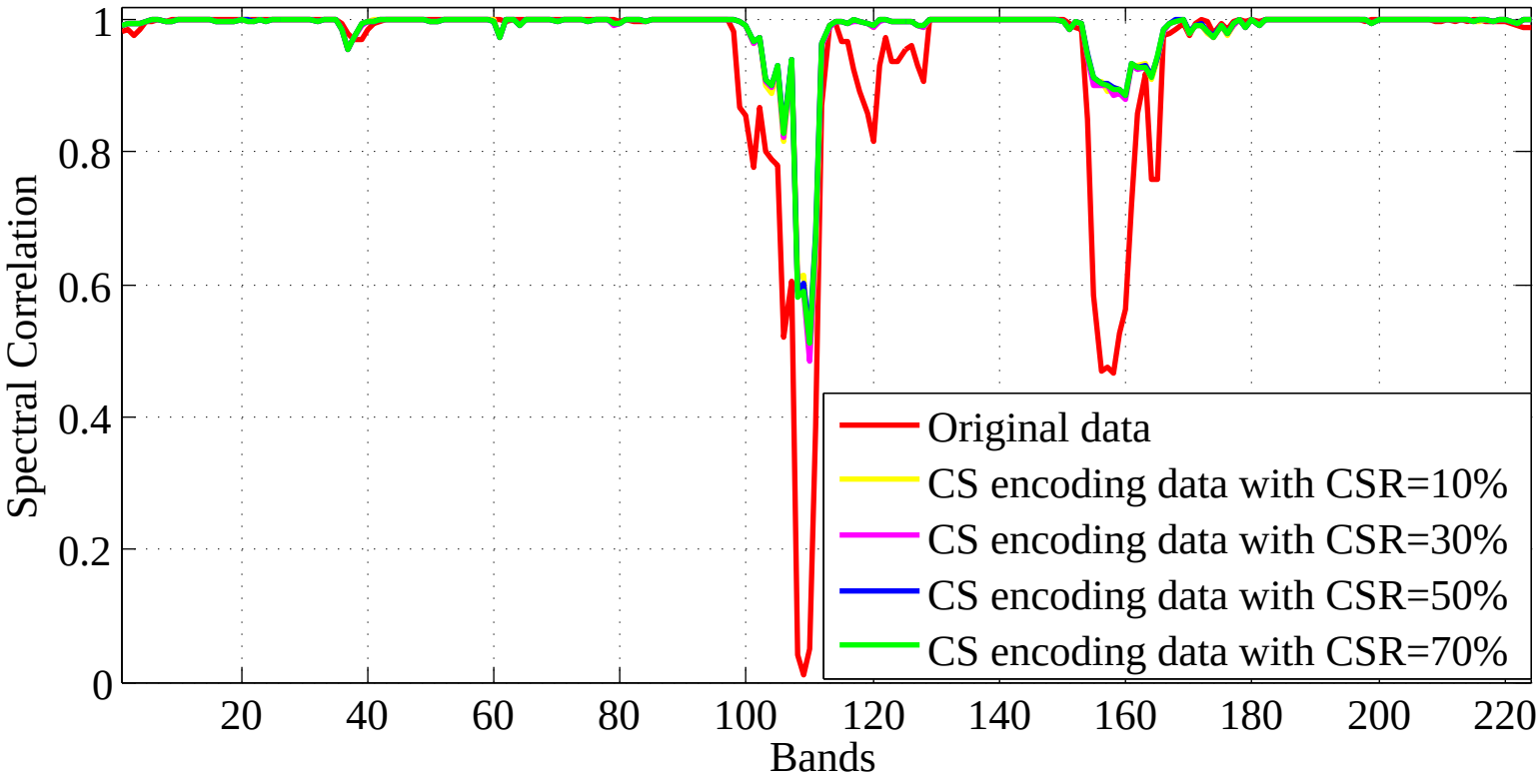
Spectral Correlation
1
0.8
0.6
0.4
0.2
0
20
40
60
80
100
120
140
160
180
200
220
Bands
Original data
CS encoding data with CSR=10%
CS encoding data with CSR=30%
CS encoding data with CSR=50%
CS encoding data with CSR=70%

Fig.4

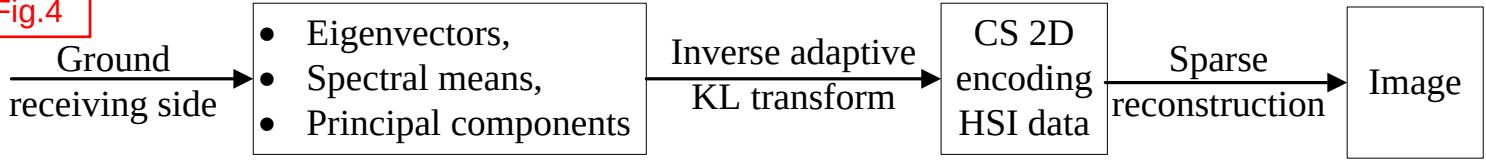
Ground
receiving side
Eigenvectors,
Spectral means,
Principal components
Inverse adaptive
KL transform
CS 2D
encoding
HSI data
Sparse
reconstruction
Image

Fig.5

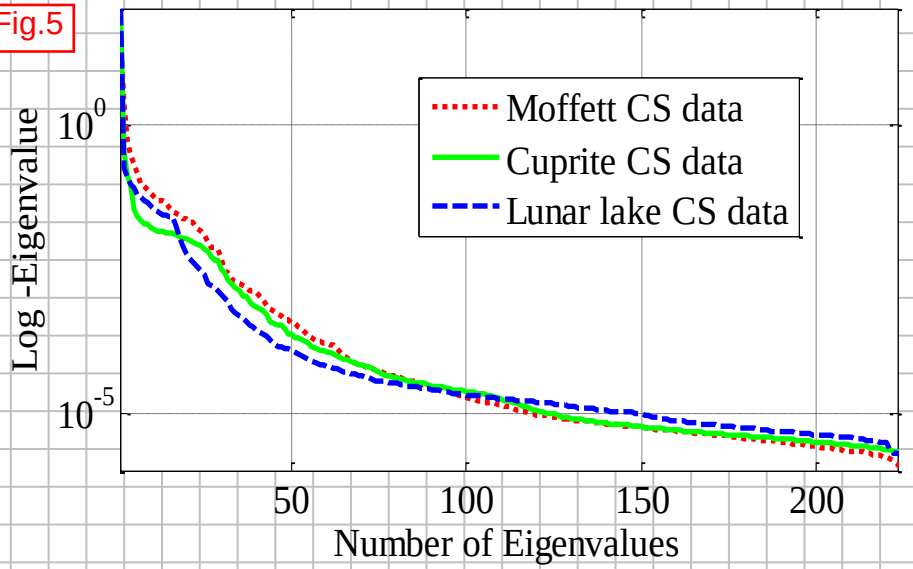
Log -Eigenvalue
10^{0}
10^{-5}
Moffett CS data
Cuprite CS data
Lunar lake CS data
50
100
150
200
Number of Eigenvalues

a

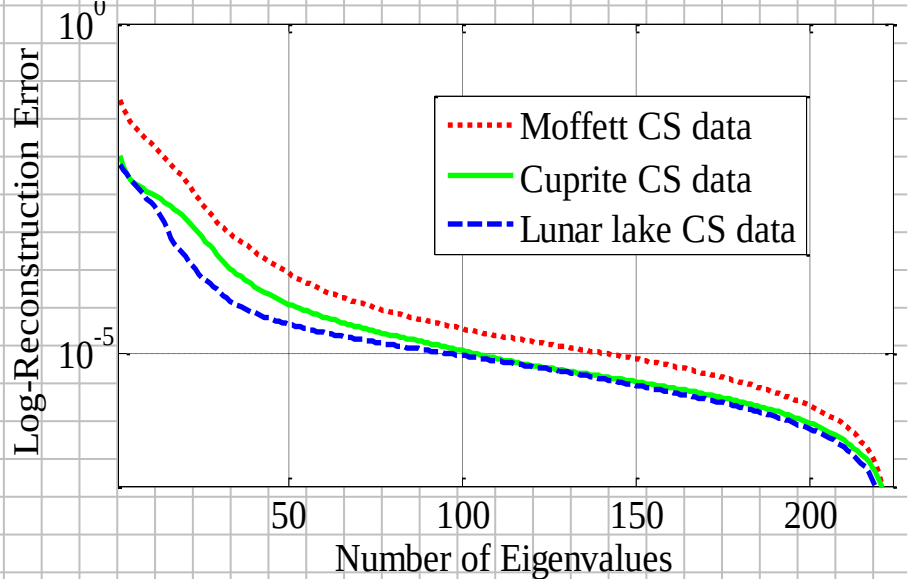
Log-Reconstruction Error
10^{0}
10^{-5}
Moffett CS data
Cuprite CS data
Lunar lake CS data
50
100
150
200
Number of Eigenvalues

b

Fig.6

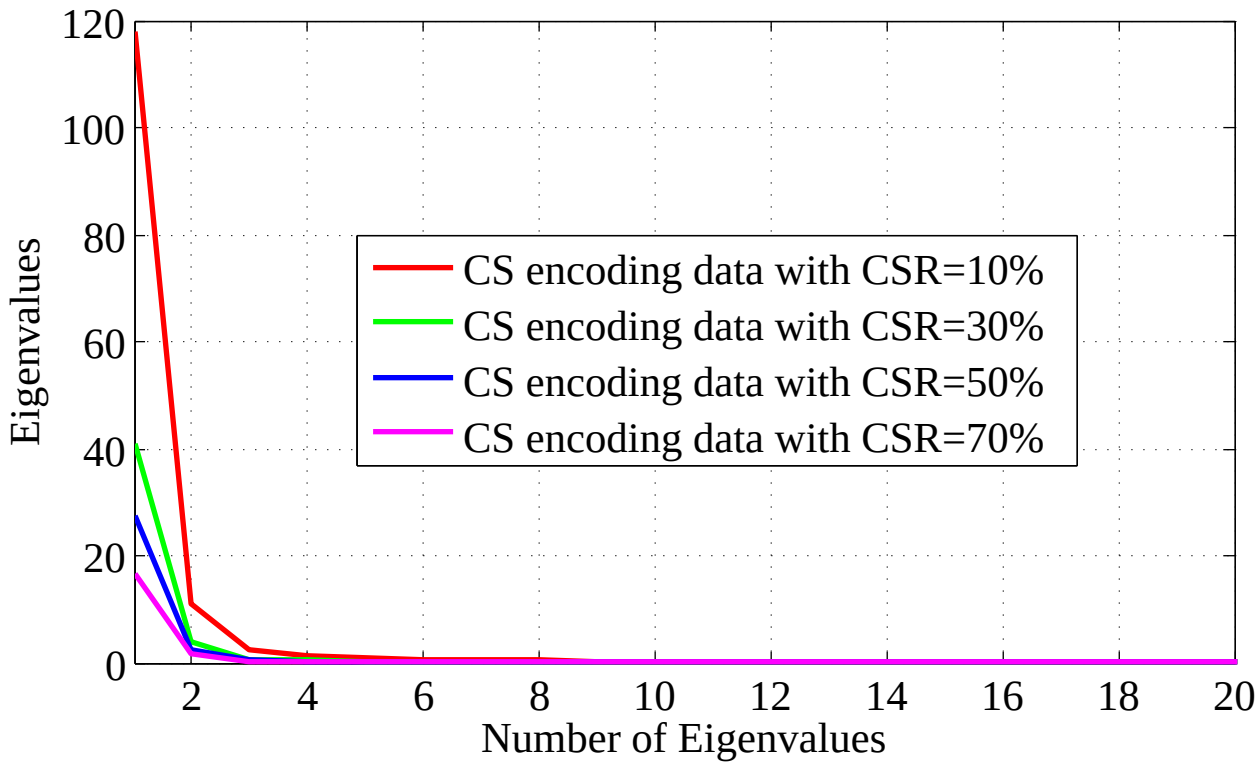
120
100
80
60
40
20
0
Eigenvalues
2
4
6
8
10
12
14
16
18
20
Number of Eigenvalues
CS encoding data with CSR=10%
CS encoding data with CSR=30%
CS encoding data with CSR=50%
CS encoding data with CSR=70%

Fig.7

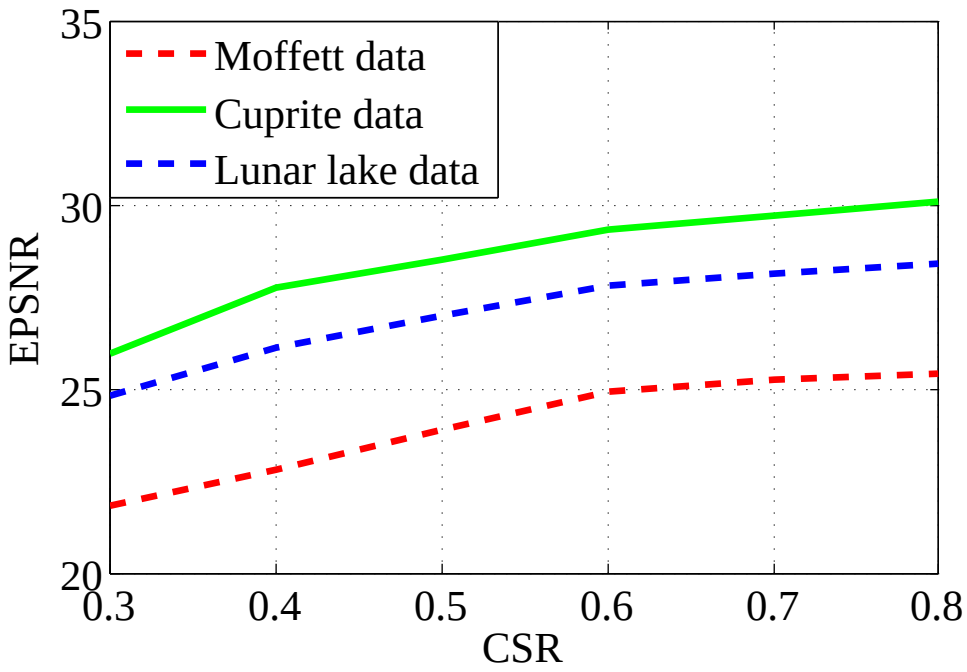
Moffett data
Cuprite data
Lunar lake data
EPSNR
CSR
35
30
25
20
0.3
0.4
0.5
0.6
0.7
0.8

Fig.8

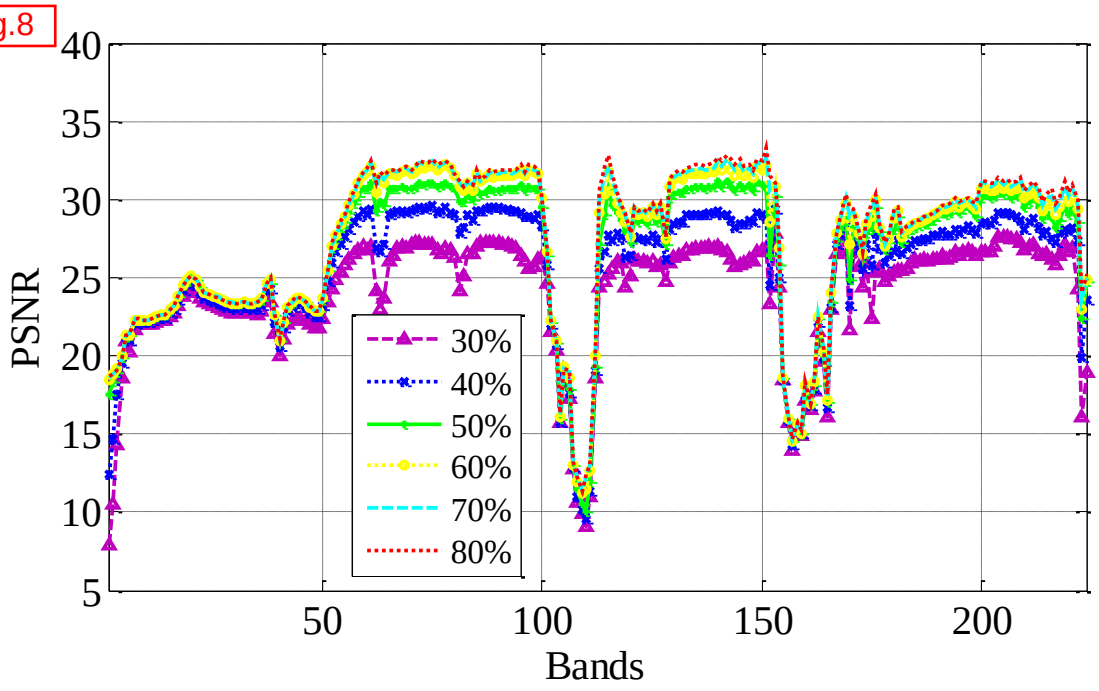
PSNR
Bands
30%
40%
50%
60%
70%
80%

a

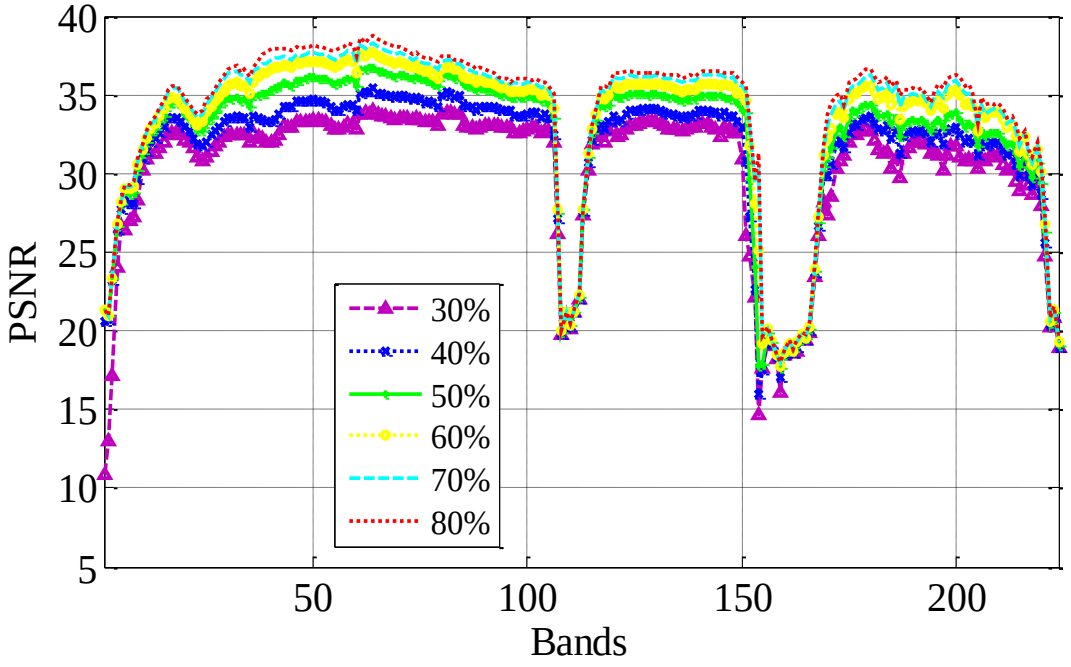
PSNR
Bands
30%
40%
50%
60%
70%
80%

b

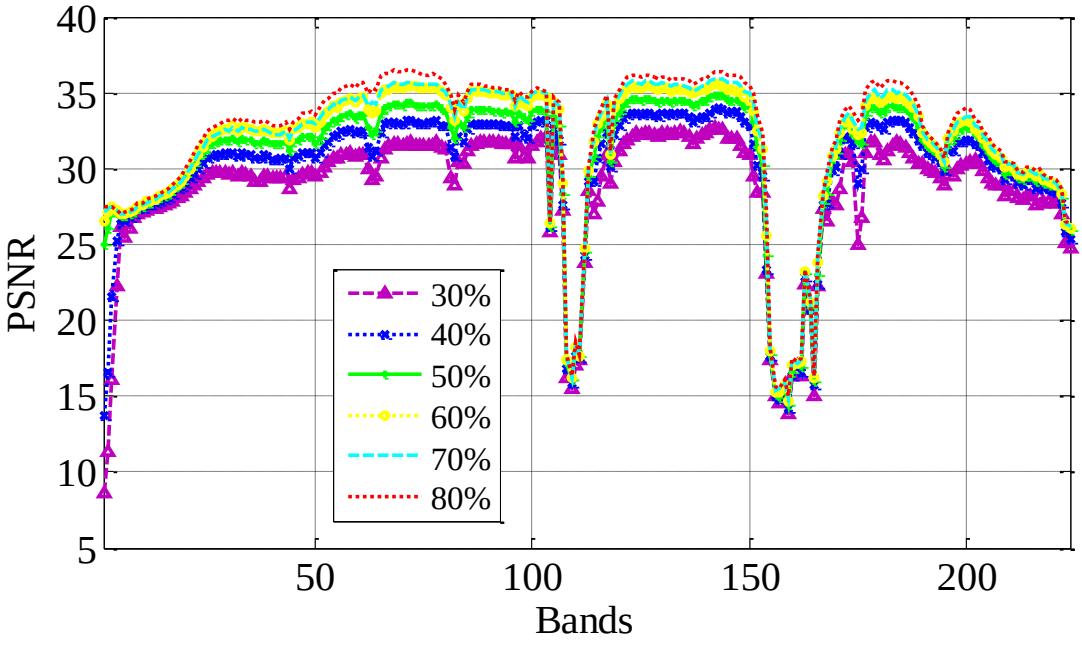
PSNR
Bands
30%
40%
50%
60%
70%
80%

c

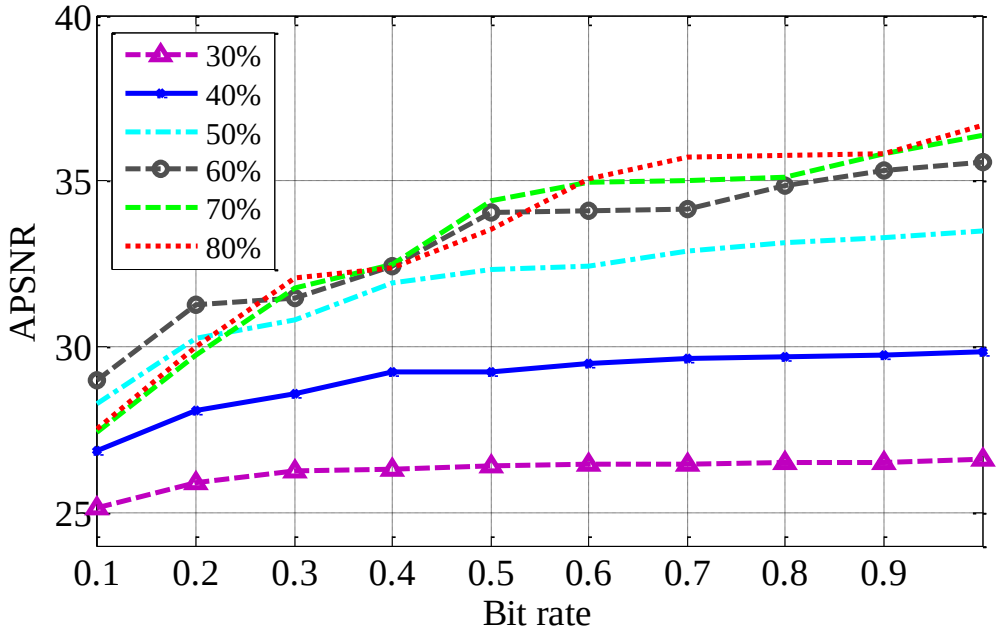
30%
40%
50%
60%
70%
80%
APSNR
Bit rate
40
35
30
25
0.1
0.2
0.3
0.4
0.5
0.6
0.7
0.8
0.9

a

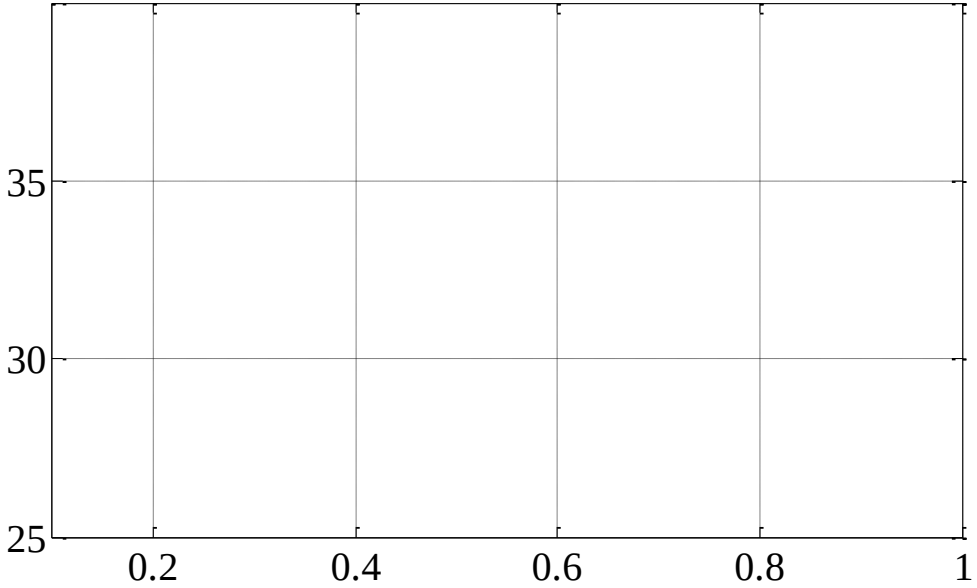
35
30
25
0.2
0.4
0.6
0.8
1

b

Fig.9

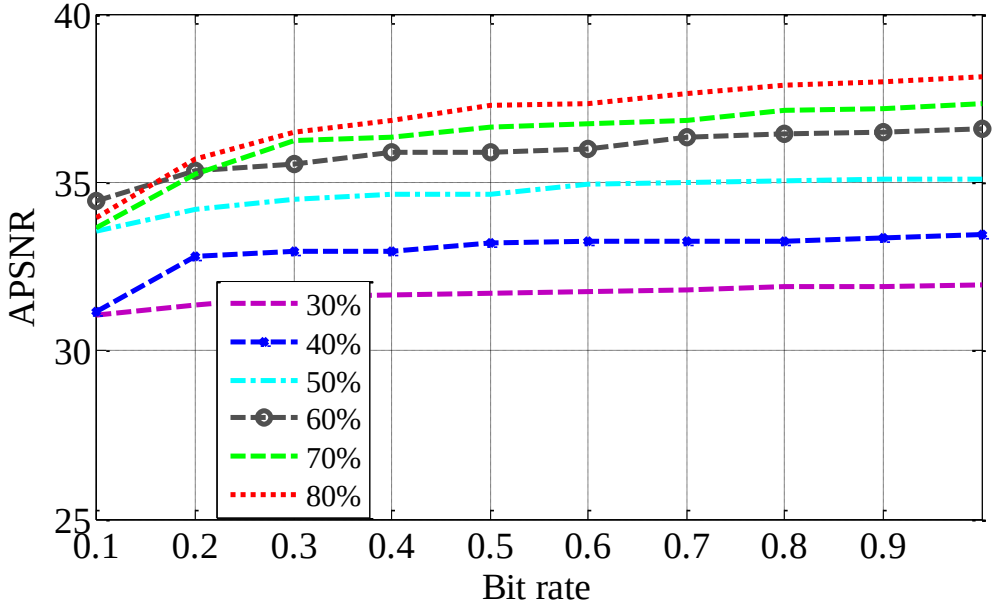
30%
40%
50%
60%
70%
80%
APSNR
Bit rate
40
35
30
25
0.1
0.2
0.3
0.4
0.5
0.6
0.7
0.8
0.9

c

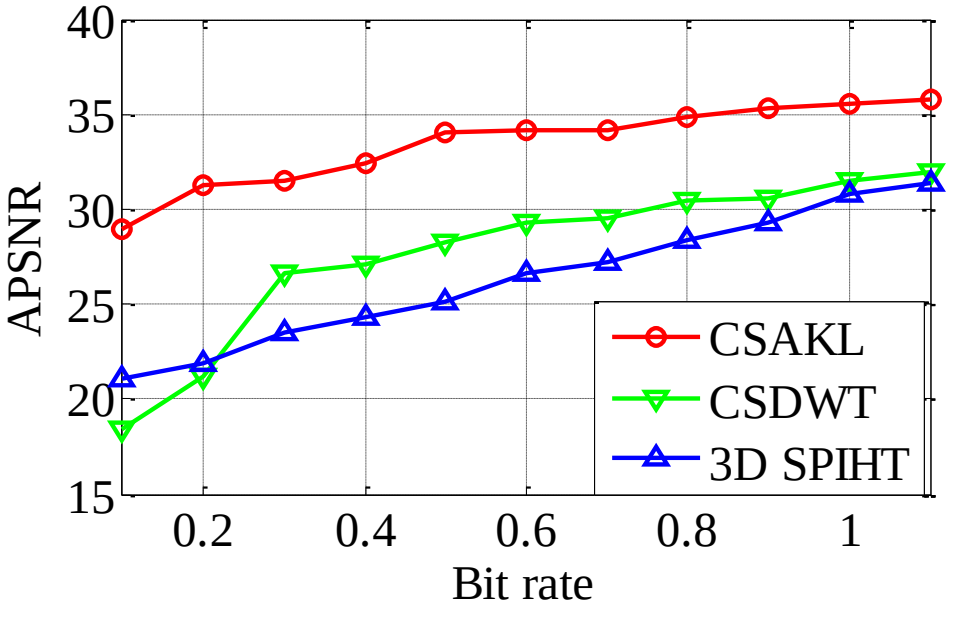
APSNR
Bit rate
CSAKL
CSDWT
3D SPIHT

a

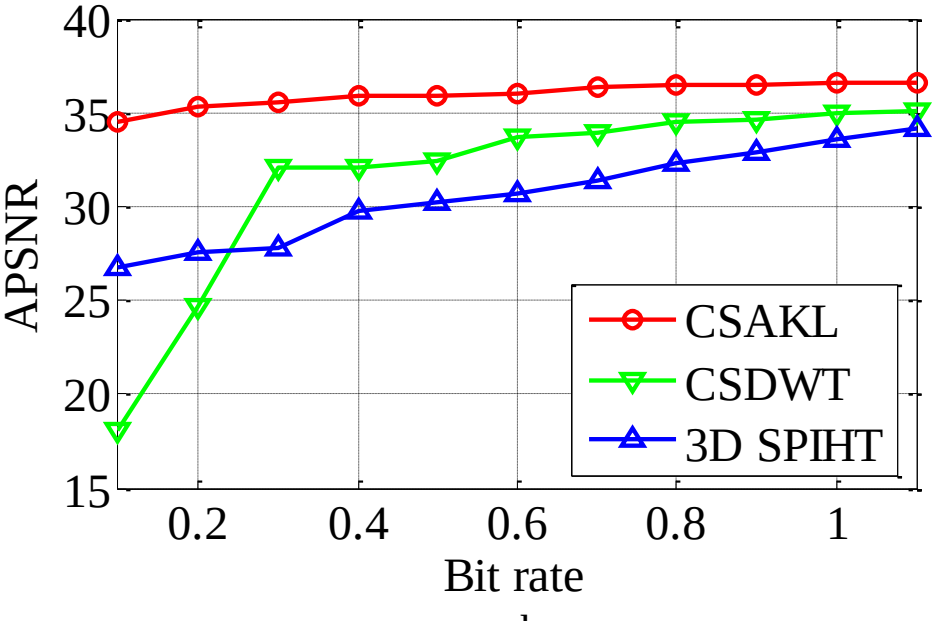
APSNR
Bit rate
CSAKL
CSDWT
3D SPIHT

b

Fig.10

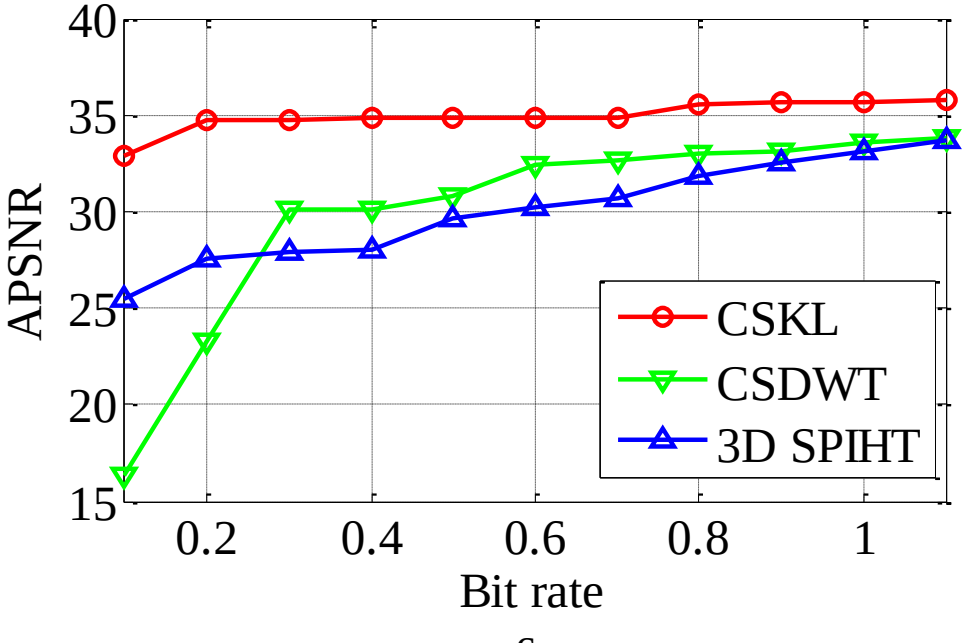
APSNR
Bit rate
CSKL
CSDWT
3D SPIHT

c

Fig.11

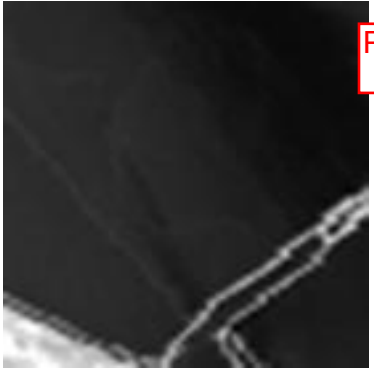

a

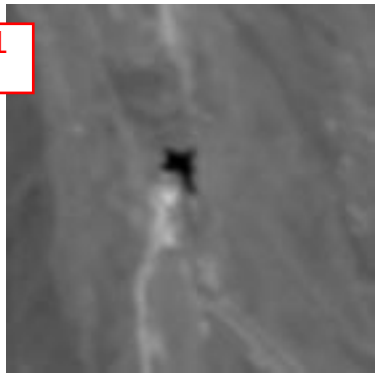

b

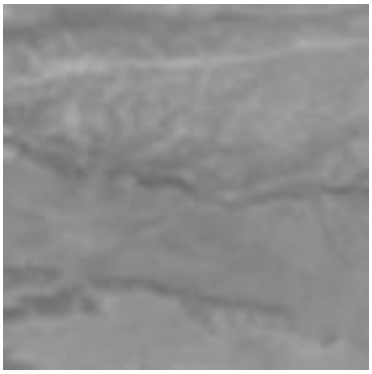

c

d

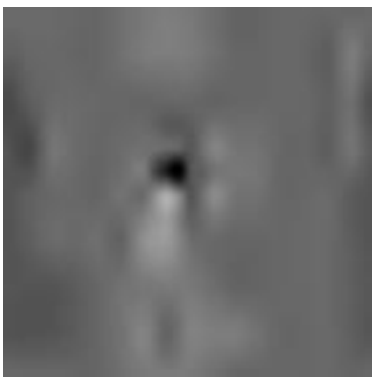

e

f

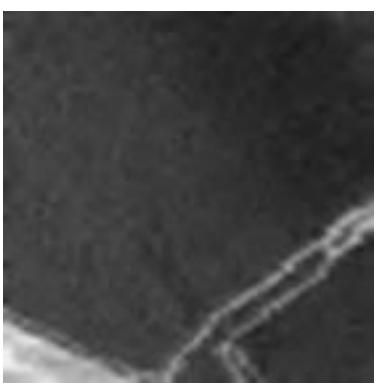

g

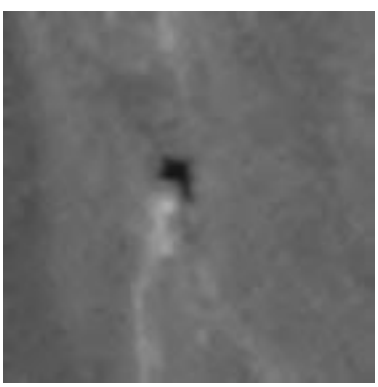

h

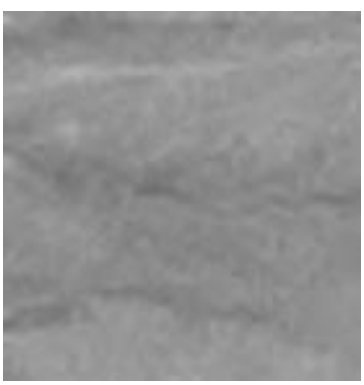

i

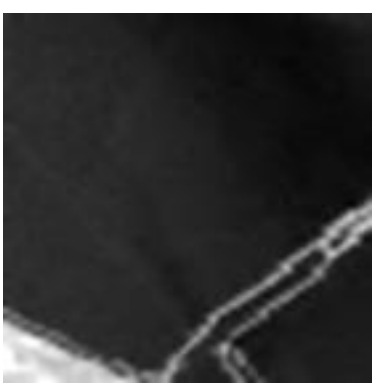

j

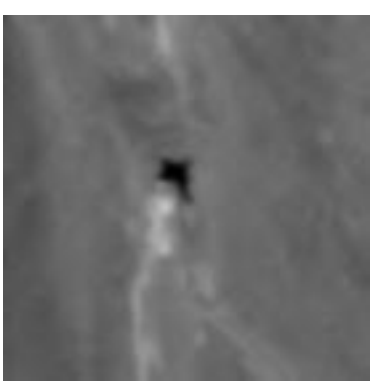

k

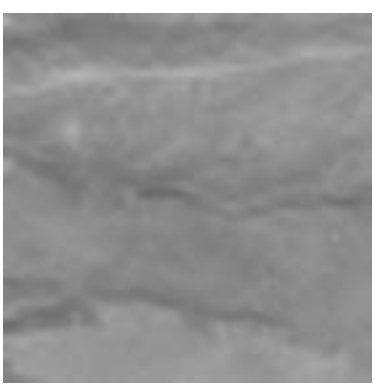

l

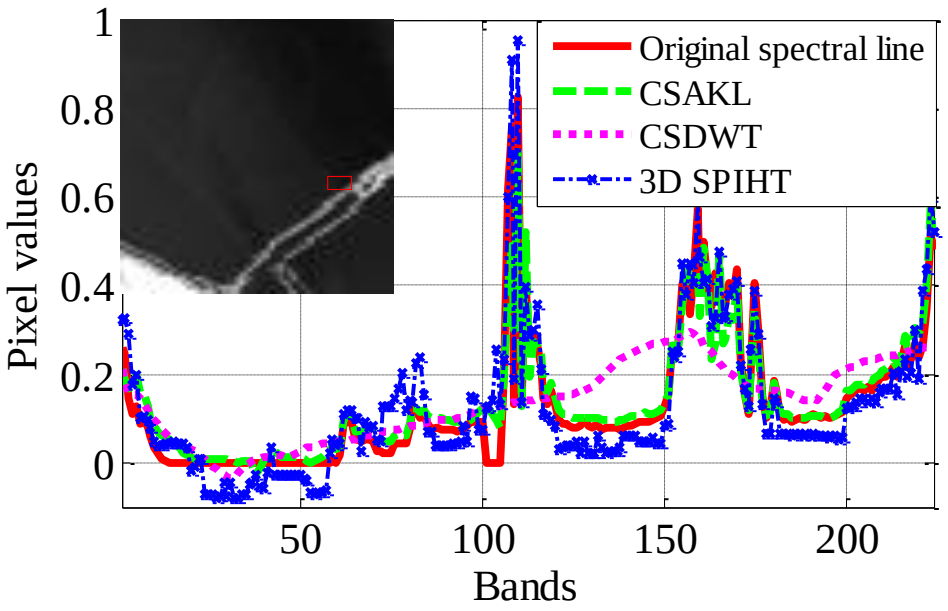
Original spectral line
CSAKL
CSDWT
3D SPIHT
Pixel values
Bands
1
0.8
0.6
0.4
0.2
0
50
100
150
200

a

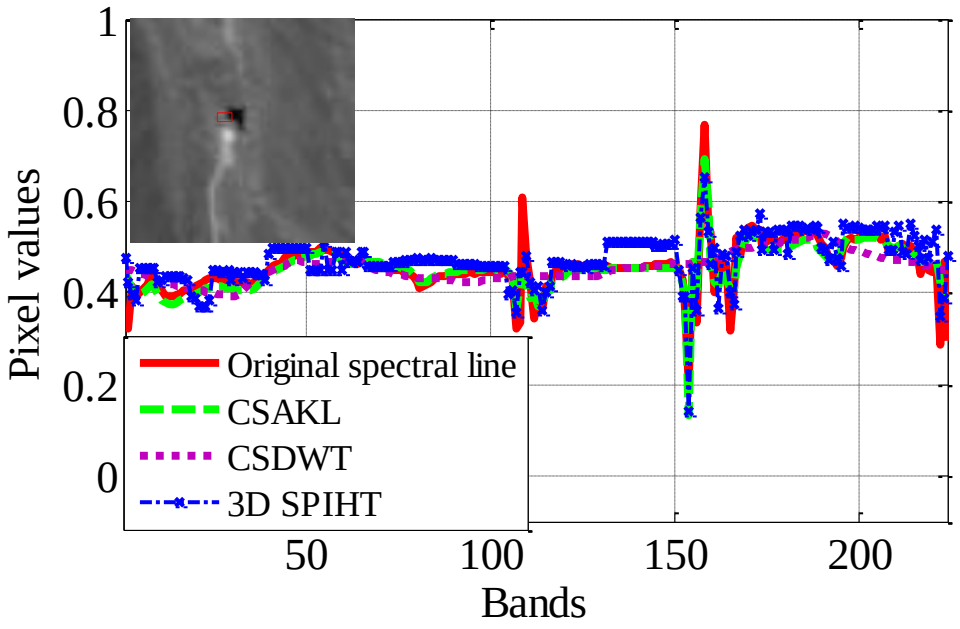
Original spectral line
CSAKL
CSDWT
3D SPIHT
Pixel values
Bands
1
0.8
0.6
0.4
0.2
0
50
100
150
200

b

Fig.12

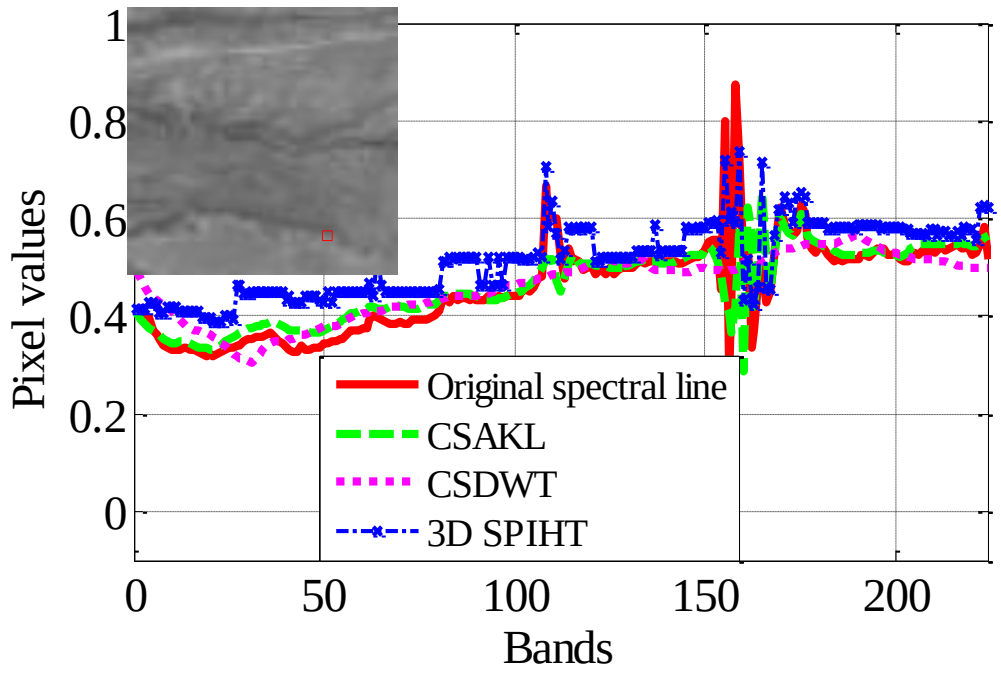
Original spectral line
CSAKL
CSDWT
3D SPIHT
Pixel values
Bands
1
0.8
0.6
0.4
0.2
0
0
50
100
150
200

c